Experimental Investigation of Wall Material Effects in Electron Cyclotron Resonance Thrusters

IEPC-2025-452

Presented at the 39th International Electric Propulsion Conference, Imperial College London, London, United Kingdom
14-19 September 2025

Ari J. Eckhaus* and Benjamin A. Jorns†
University of Michigan, Ann Arbor, MI, 48103, USA

The effects of wall material on the plasma properties of an ECR magnetic nozzle thruster are experimentally characterized. Multiple configurations of a 30 W-class ECR thruster are tested, including changes to the material of the plasma source walls and surrounding thruster body. Each variation is tested at 1 SCCM-Xe with input powers ranging from 20 W to 50 W. Thruster global performance is directly measured using a thrust stand, and specific impulse and total efficiency are calculated from these measurements. Far-field plasma properties are measured using a diagnostic suite consisting of a Langmuir probe, Retarding Potential Analyzer, Faraday probe, and ExB probe. Results suggest that use of electrically insulating materials for the radial wall of the source region and thruster body increases thrust by as much as 20 %. Efficiency mode analysis shows that conductive materials increase plasma losses to the walls, resulting in decreased mass utilization and energy efficiencies. For the material of the source region backplate, SEE is suspected to impact device behavior along with the dielectric strength of the material. These effects combine to decrease the mass utilization and energy efficiency of the device when the boron nitride backplate is changed to aluminum oxide. The characterization of these thruster configurations indicates optimized performance when electrically insulating material with low SEE are used.

I. Introduction

As the scientific capabilities of small satellites continue to increase, the need for efficient, low-power electric propulsion (EP) becomes more pressing.[1,2] One of the most promising technologies to fill this gap in the EP landscape is the Electron Cyclotron Resonance (ECR) Magnetic Nozzle thruster. These devices utilize a highly effective heating scheme to couple microwave energy into the electrons of a plasma. A diverging magnetic field then converts the electron thermal energy into ion kinetic energy through an ambipolar diffusion process. This principle of operation offers several advantages for small satellite propulsion. Firstly, the efficiency of ECR heating allows these thrusters to maintain a stable plasma discharge at powers <100W. Second, because the ambipolar acceleration mechanism of the magnetic nozzle maintains quasineutrality, ECR Magnetic Nozzle thrusters eliminate the requirement for a neutralizer hollow cathode. This electrodeless operation offers potential lifetime advantages and system-level simplicity compared to other mature EP technologies.[3] Largely due to these prospective advantages, low-power ECR Magnetic Nozzle thrusters have become an increased research focus over the past decade.[4–7]

In 2013, the Office National d'Etudes et de Recherches Aérospatiales (ONERA) introduced an ECR Magnetic Nozzle thruster designed to operate at 50 W.[5] Although this early prototype was promising, the maximum efficiency observed was 3.5%. Since then, the low-power, coaxial ECR thruster architecture has been studied by several international groups. Thruster performance has been characterized when operating with various microwave frequencies, magnetic field topologies, propellants and source region dimensions and materials.[6–8] In 2022, the insights gained through these experiments led to the development of a test article at ONERA that demonstrated $> 40\%$ efficiency when operating at 30 W.[8]

*Ph.D Candidate, Aerospace Engineering, aeckhaus@umich.edu
†Associate Professor, Aerospace Engineering

Although prior optimization efforts were successful in increasing overall thruster performance, many of the physical mechanisms that enabled these improvements remain poorly understood. One example relates to the materials used in the plasma source region of the thruster. In one test, it was observed that thrust increased by 20% when the walls of the ECR source region were coated with a dielectric film.[9] We previously found similar thrust trends when a device was tested with walls of various materials, including aluminum, graphite, and boron nitride.[10] To gain insight into the plasma behavior, we also regressed these results against a quasi-1D model. However, plasma properties were not directly measured. As a result, the effects of wall material on plasma properties of the thruster remain undetermined.

Two physical processes have been proposed to explain the relationship between material of the thruster components and plasma behavior. The first hypothesis relates to the electrical conductivity of the material. This theory suggests that electrically conductive walls may allow non-local currents to form in the plasma, thereby increasing losses to the walls of the source region or thruster body.[11,12] The second theory considers secondary electron emission (SEE). Secondaries emitted from the walls may act as "donor electrons", which could replenish wall losses. Additionally, these secondary electrons can be reheated by ECR and serve to ionize propellant and help establish the ambipolar acceleration process.[13] However, SEE also reduces the sheath potential drop at the thruster walls.[14,15] This would allow the plasma to reach the wall more easily, resulting in higher losses. Because these proposed processes can result in both beneficial and detrimental effects on thruster performance, it is difficult to assess how wall material affects plasma behavior based on global performance trends. Instead, characterizing the physical implications of wall material effects requires direct measurements of plasma properties.

The goal of this effort is to perform these direct measurements and evaluate the hypotheses that relate wall material to thruster performance. To do so, we test several thruster configurations, including material changes to the radial walls, back wall, and thruster body. For each configuration, we utilize a far-field probe suite to measure changes in plasma properties of the ECR thruster. With this goal in mind, this paper is organized as follows. Sec. II provides an overview of the thruster operation and elaborates on the hypotheses relating to wall material effects. In Sec III we present the framework used to evaluate thruster performance and relate plasma properties to global performance metrics. Sec. IV describes the experimental setup used in this investigation, including the various thruster configurations tested. Sec. V presents the results of our experimental characterization, followed by a discussion of the relationship between wall material and plasma properties in Sec. VI. Finally, in Sec. VII we summarize our findings and describe the implications of these results for the operation of the ECR thruster.

II. Principle of Operation of ECR Magnetic Nozzle Thrusters

ECR thrusters operate by first heating the electrons of a plasma and subsequently converting this electron thermal energy into directed ion kinetic energy using a magnetic nozzle. We show a diagram of the typical thruster geometry in Fig. 1.

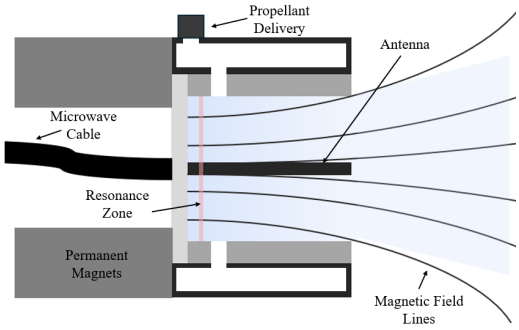

Figure 1. Canonical Geometry of a Coaxial ECR Magnetic Nozzle Thruster

Key components of the device include permanent magnets to establish the magnetic nozzle, a radial gas plenum and propellant injection scheme, and a plasma source region that is bounded by a cylindrical radial wall and a circular backplate. The thruster we use in this work leverages a coaxial power coupling scheme similar to the low-power devices studied by ONERA.[4,5,8] The characteristic feature of this design is the

central antenna, which deposits RF power into the plasma. This direct coupling near the antenna is suspected to result in stronger peak electric fields and higher electron temperatures and has been proposed as the reason for improved performance of coaxial ECR thrusters compared to early waveguide concepts.[16–18].

To initiate a plasma discharge, propellant is injected to the source region through the radial manifold. In this neutral gas, there exists a small fraction of free electrons. As these electrons interact with the magnetic field in the source region, they undergo cyclotron motion. At the same time, microwaves are injected through the central antenna, with the walls of the plasma source serving as a wave guide. In a small area of the plasma source region, the so-called "resonance zone", the electron cyclotron resonance condition is matched. This occurs when the angular frequency of the injected microwaves, ω_{rf} matches the electron cyclotron frequency, ω_{ce}:

$$\omega_{RF} = \frac{f}{2\pi} = \frac{qB}{m_e} = \omega_{ce}. \tag{1}$$

Here f is the linear frequency of the microwave, q is the electron charge, B is the magnitude of the magnetic field strength, and m_e is the mass of the electron. This resonance interaction effectively deposits microwave power into the electrons. It has been experimentally shown that ECR heating can deposit over 90% of input power into the plasma.[19] The hot electrons then collide with surrounding neutral gas atoms, resulting in ionization. This ionization yields more free electrons, which themselves are heated through resonance and maintain ionization.

The hot, highly mobile, electrons stream away from the source region and follow the magnetic field lines downstream. This creates a charge imbalance as the cold, heavy, ions remain. The result is an electric field that accelerates the ions downstream to maintain quasi-neutrality. In this way, the electron motion is coupled to ion motion and the ions are accelerated to high velocities. However, if the plasma were to remain attached to the diverging field lines of the magnetic nozzle, it would return to the back of the thruster. Therefore, the plasma must detach from the diverging field lines. The physical mechanism of this detachment process is an active area of research.[20–22] However, characterizations of ECR thrusters, including this work, have found that the plasma detaches from the magnetic nozzle before plume divergence becomes a dominant loss.[23]

With an understanding of the ECR thruster principle of operation, we can now examine the theoretical reasons behind the effects of wall conductivity and secondary electron emission.

A. Theoretical Effects of Wall Electrical Conductivity

The typical magnetic field topology of an ECR magnetic nozzle thruster is shown in Fig. 1. We see that there is a strong magnetic field ($>$ 800G), which, in principle, serves to confine the plasma away from the walls. This field is strong enough to fully magnetize the electrons such that they have limited mobility in the radial direction. However, along magnetic field lines, the electrons are highly mobile and can therefore stream to the walls in the axial direction. Conversely, the ions are not magnetized and may cross field lines radially. This asymmetry in diffusivity between the species of the plasma is critical to understanding how wall conductivity affects loss mechanisms in the ECR thruster. Because the entire device is electrically

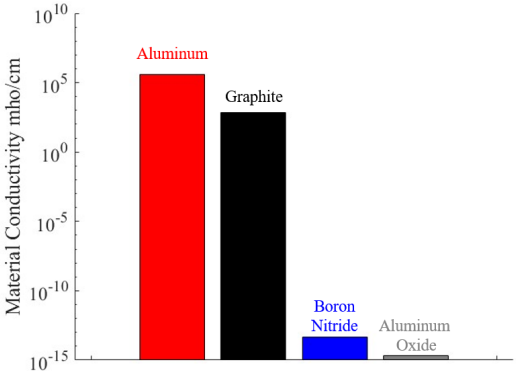

Figure 2. Electrical conductivities of the materials tested

floating, the walls of the thruster must maintain a zero net current condition. Walls made of electrically conductive materials are able to carry current, which allows non-local losses of ions and electrons to offset. This phenomenon, known as a "Simon Short Circuit", increases the total plasma losses to the walls and has proven to be detrimental to performance of ECR ion sources.[11,12] In cases where the walls are insulating, the diffusion to the walls must be driven by slower, ambipolar diffusion. Therefore it is suspected that insulating walls improve plasma confinement and reduce wall losses. In our experiments, we expect this difference to appear in two efficiency modes: mass utilization and energy efficiency. The increased wall losses arising from Simon Short Circuits should cause a decrease in plasma density and greater power losses. These effects will cause a decrease in both mass utilization and energy efficiency and likely result in lower overall performance of the thruster compared to tests with insulating walls. To assist in our evaluation of this hypothesis, we plot in Fig. 2, the electrical conductivities of the materials studied in our investigation.

B. Theoretical Effects of Wall Secondary Electron Emission

In the ECR thruster, secondary electron emission occurs when high-energy electrons impact the walls of the source region. The number of secondaries emitted depends on both the energy of the incident electrons and the wall material. This relationship is quantified through the material's secondary electron yield, which is the ratio between emitted and incident electrons. We plot in Fig. 3 the secondary electron yield as a function of incident electron temperature for the materials studied in this work.

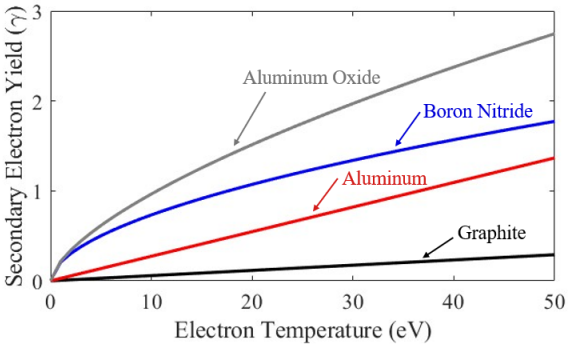

Figure 3. Secondary electron yield of the materials tested[15,24,25]

SEE in ECR devices has been proposed to cause two competing effects. First, in ECR sources for controlled fusion, experiments found higher ion current output and improved device stability when the walls of the plasma chamber were coated with an oxide layer. This behavior was attributed to SEE of the walls.[13] Specifically, it was suggested that the walls acted as an electron source in the plasma, thereby increasing electron density and improving ionization fraction. Considering this "donor electron" hypothesis in the context of ECR thrusters, we would expect this effect to result in higher global performance for wall materials with higher SEE. Physically, this would result in an increased total ion current, which can be measured with our far-field Faraday probe. Correspondingly, in our efficiency breakdown, the suspected improved ionization fraction should manifest as an increase to mass utilization efficiency.

The second, well-characterized, effect of wall SEE involves changes to the sheath dynamics in the near-wall region of the plasma. The sheath serves to repel electrons and attract ions to maintain a zero net current condition on the wall. This is done by establishing an electric field that causes the wall to be biased more negative than the local plasma potential. However, in the flux balance argument, a secondary electron emitted by the wall produces the same charge as an ion reaching the wall. To offset this effect, the magnitude of the repelling sheath potential decreases, allowing more primary electrons to traverse the sheath and reach the wall.[14,15] One result of these higher electron losses is a decrease to the electron plasma density in the source region, which will inhibit ionization and decrease the mass utilization efficiency mode. Another consequence of these wall losses is that the electrons lost in the source region have not yet traversed the magnetic nozzle and deposited their energy into the ions. Therefore the RF power that was coupled into the electrons is also lost. In our efficiency breakdown, we expect this increased power loss to the walls will appear as a decrease in energy efficiency.

III. Approach to Quantifying Thruster Performance

We begin this section by discussing global performance metrics for propulsion systems. We then establish a framework for evaluating thruster performance and relating global performance metrics to plasma properties through an efficiency breakdown.

1. *Global Performance Metrics*

The primary diagnostics we employ in this work are the thrust, T, mass flow rate, $\dot{m}$ and power to the engine, P. Subject to these measurements, we in turn can evaluate the specific impulse and total efficiency for the system:

$$I_{sp} = \frac{T}{\dot{m}g} \qquad \eta = \frac{T^2}{2\dot{m}P}, \tag{2}$$

where g is the acceleration due to Earth's gravity at sea-level. The former in the above expression is an indication of the propellant efficiency of the system while the latter represents the efficacy of conversion of external power into directed thrust.

2. *Efficiency Breakdown*

Although global performance metrics provide valuable information about the overall behavior of EP devices, they fail to provide detailed information about changes to the physical properties of the plasma. To gain additional insight into plasma behavior, it is common to relate global performance to thruster plasma properties through an efficiency breakdown.[7,9,23] In this approach the total efficiency, described by Eq. 2, is broken into several sub-efficiency modes. For ECR thrusters, three efficiency modes are commonly employed:

$$\eta = \eta_m \eta_d \eta_e, \tag{3}$$

where η_m is the mass utilization efficiency, η_d is beam divergence efficiency, and η_e is energy efficiency. We describe each efficiency mode in detail in the following sections.

Mass Utilization Efficiency

Mass utilization efficiency compares the flow rate of ions out of the thruster, $\dot{m}_i$, to the flow rate of neutrals into the thruster. We express this in terms of plasma properties measured in the far-field of the thruster as

$$\eta_m = \frac{\dot{m}_i}{\dot{m}} = \frac{I_{tot} m_i}{q\dot{m}} \sum_n \frac{\Omega_n}{Z_n}, \tag{4}$$

where m_i is the ion mass, q is the fundamental charge, Z_n is the charge state of species, n, Ω_n is the fraction of ions in charge state, n, in the beam, and I_{tot} denotes the total ion current emitted from the device.

Divergence Efficiency

Of the high-velocity plasma emitted by the thruster, thrust is only generated by momentum exchange along the axis of the thruster. Therefore, any component of the beam velocity that is not along the thrust axis represents a performance loss. This loss is captured by

$$\eta_d = \cos(\lambda)^2, \tag{5}$$

where we have defined

$$\lambda = \operatorname{acos}\left(\frac{I_{ax}}{I_{tot}}\right).$$

This is the characteristic divergence half-angle, of the plume, which represents the ratio of axially directed ion current, I_{ax}, to total ion current.

Energy Efficiency

The final efficiency mode considered in our analysis, energy efficiency, indicates the conversion of electrical power into ion kinetic power:

$$\eta_e = \frac{P_i}{P} = \frac{E_i I_{tot}}{P}, \tag{6}$$

where E_i denotes the downstream ion energy. In practice, this expression for energy efficiency encompasses a variety of loss processes associated with both the source region and the acceleration processes in the magnetic nozzle. Although these loss processes could be separated into more granular efficiency modes, difficulties associated with probing the near-field of the thruster limit our ability to further refine this energy efficiency term.[7,26,27]

IV. Experimental Setup

In this section we describe the experimental setup we used for our investigation. This includes information about the facility, test article and infrastructure. We also discuss our methods for ensuring repeatability of our data. We then detail the plasma diagnostics we used in this work to measure the properties required for our efficiency mode analysis.

A. Facility

We performed all experiments for this effort in the Junior test facility at the University of Michigan's Plasmadynamics and Electric Propulsion Laboratory (PEPL). Junior is a 1 m diameter by 3 m long chamber with a pumping speed of 32,000 L/s on xenon. During this experimental campaign base pressures varied from 2-5 μTorr-N_2.

B. Thruster

The thruster we used in this work is the PEPL ECR VII test article. A cross section of the thruster is shown in Fig. 4. This device was designed to have modular components, allowing us to easily test multiple thruster configurations. These variations are described in detail in the following subsections.

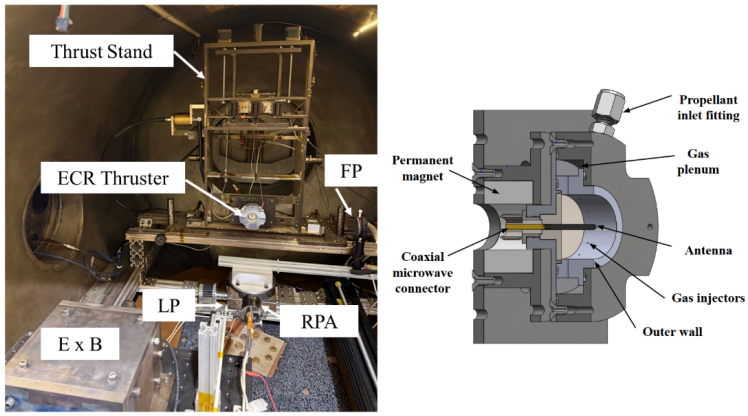

Figure 4. Left) Far-Field probe suite and ECR thrust stand installed in the Junior test facility Right) Cross section of the UM ECR VII thruster

1. *Baseline Configuration*

Much of the previous characterization of the UM ECR VII thruster was done with an aluminum radial wall, boron nitride backplate, graphite antenna, and an anodized aluminum body.[6] Therefore, in this work, we consider this to be the "baseline" configuration. Starting from the baseline, we then vary the materials of the radial wall, backplate, and thruster body. During these studies, we keep all other components in their baseline configuration. This test matrix is summarized in Fig. 5.

	Radial Wall Study				Backplate Study		Thruster Body Study	
Radial Wall	**BN**	**Al_2O_3**	**Al**	**C**	Al	Al	Al	Al
Backplate	BN	BN	BN	BN	**BN**	**Al_2O_3**	BN	BN
Thruster Body	Anodized	Anodized	Anodized	Anodized	Anodized	Anodized	**Anodized**	**Untreated**
Antenna	C	C	C	C	C	C	C	C

Figure 5. Wall Material Effect Test Matrix. The focus of the study is highlighted in the column headings, rows represent the material of each component.

2. Variation to Radial Wall Material

We show in Fig. 6 the thruster equipped with various radial wall materials. In this study, we test the thruster with walls made of aluminum, graphite, boron nitride (BN) and aluminum oxide (alumina). Unlike our previous efforts to characterize radial wall material effects,[10] the ceramic walls are manufactured entirely from the base material, rather than applying a coating. This was done to avoid complications from coating degradation and microwave coupling to the conductive base material. When testing variations in radial wall material, the backplate, antenna, and body material remained in the baseline configuration as boron nitride, graphite, and anodized aluminum respectively.

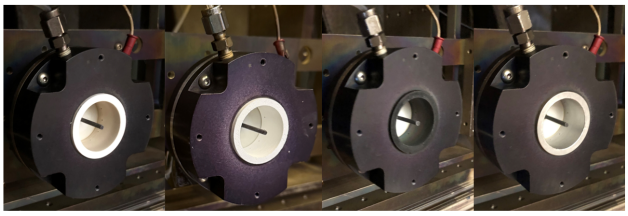

Figure 6. UM ECR VII thruster shown with radial walls of (a) Boron Nitride (b) Aluminum Oxide (c) Graphite and (d) Aluminum

3. Variation to Backplate Material

As shown in Fig. 4, the thruster backplate serves to both confine the plasma and also provides an entry point for the antenna into the source region. Because it contacts the antenna, the backplate material must be insulating to avoid shorting the microwave delivery circuit. Therefore, we manufacture backplates of the two insulating materials from the previous section: alumina and boron nitride. When testing variations in backplate material, aluminum radial walls were used with the anodized thruster body and the antenna material was graphite. We show, in Fig. 7, a photo of the two backplates after testing.

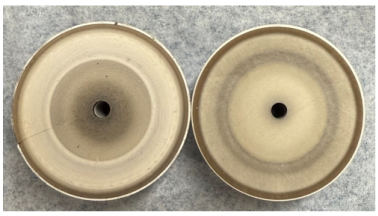

Figure 7. Thruster backplates of alumina (Left) and boron nitride (Right). Pictures are taken after approximately 5 hours of operation with aluminum walls and a graphite antenna

4. Variation to Thruster Body Material

In its baseline configuration, the body of the ECR VII thruster is made of anodized aluminum. We initially made this design decision to improve the radiative properties of the device.[6] However, this process also

modifies the electrical conductivity of the material, such that the anodized thruster body is a poor electrical conductor. To investigate the effects of conductivity, we tested a second thruster body of the same base material that did not undergo anodization. This configuration is shown in Fig. 8. As with the previous tests, we keep the other thruster components unchanged during thruster body testing. These materials were aluminum radial walls, boron nitride backplate, and graphite antenna.

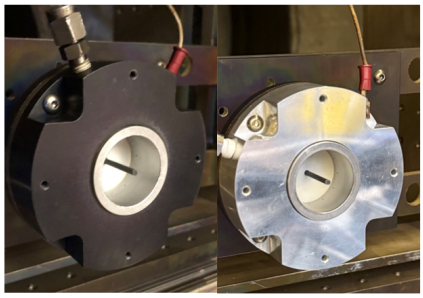

Figure 8. The tested thruster body configurations of (a) black anodized aluminum and (b) untreated aluminum

C. Thrust Stand and Thruster Infrastructure

We take direct thrust measurements of the ECR VII using the pendulum-type thrust stand shown in Fig. 4.[6] The thrust stand also contains a sense line to measure the floating potential of the thruster body and provides power and propellant delivery to the thruster inside the test facility. The microwave signal is generated by a WindFreak Synth HD pro and then amplified to the desired power setting using a Mini-Circuits ZHL-2425-250X+ amplifier. Forward and reflected power are monitored using a Mini-Circuits ZGBDC20-372HP+ bidirectional power coupler and read using an Agilent N1912A power meter. We calibrate the power meter to account for line losses inside the chamber, allowing us to estimate power delivered to the thruster. We control propellant flow using an Alicat MC-50SCCM-D mass flow controller. With this experimental setup, we are able to directly measure thrust while also monitoring power and propellant delivery. In this way we are able to determine key performance metrics of thrust, specific impulse and total thruster efficiency. Figure 4 shows the far-field probe suite installed in the Junior vacuum facility. We use a Langmuir probe (LP), Retarding Potential Analyzer (RPA), Faraday Probe (FP), and ExB probe to measure the plasma properties of the UM ECR VII thruster with various wall materials. We describe each probe in detail in the following subsections.

D. Far-Field Plasma Diagnostics

1. Langmuir Probe

Langmuir probes can be leveraged to evaluate key plasma properties such as plasma potential, ϕ and electron temperature, T_e. In this work, we utilized a cylindrical Langmuir probe consisting of a 0.381 mm diameter by 10 mm length tungsten electrode, shielded by an alumina tube. We sweep voltage on the probe from -50 V to 100 V, and measured current using a Keithley 2400 Source Meter. We took all Langmuir probe traces on thruster centerline, a distance of 50 cm downstream from the exit plane. We estimate the Debye length, λ_D, at this distance to be approximately 0.5 mm, suggesting that thin sheath theory is not valid for this probe. Instead, we use OML sheath theory to analyze the Langmuir probe.[28] We use multiple methods to identify plasma potential, including the first and second derivative techniques as well as a logarithmic fitting technique. To assess uncertainty, LP trace is taken three times and plasma potential is determined using the techniques described. We then take the average of these calculated plasma potentials and use the standard deviation of these values to assess the error in our calculation.

2. Retarding Potential Analyzer

A Retarding Potential Analyzer uses a series of charged grids to repel plasma species and monitor current on a collector behind the grids. By sweeping the voltage of the ion retarding grid and monitoring collected

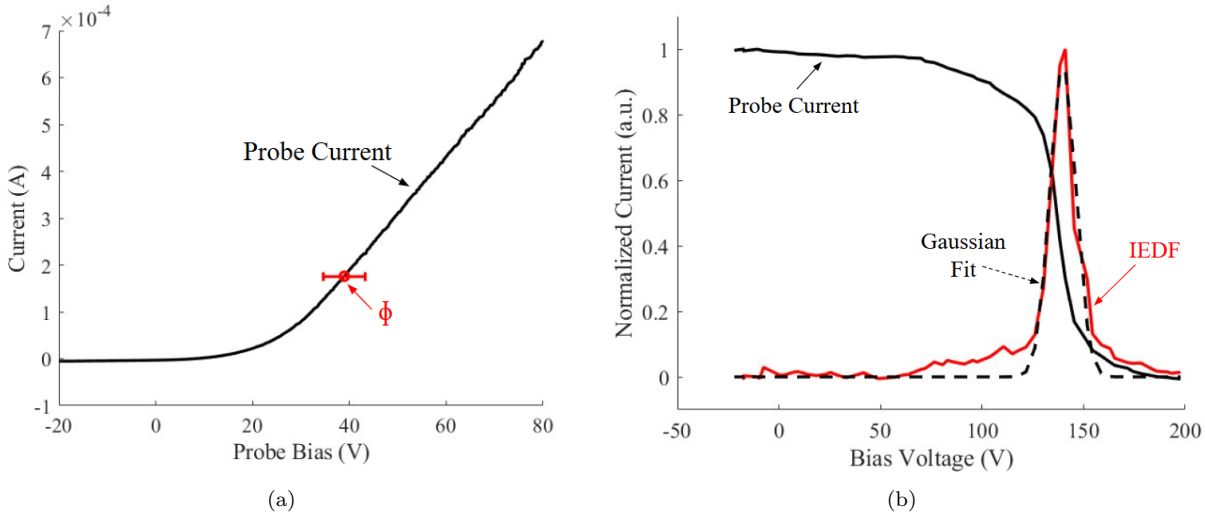

Figure 9. (a)Sample Langmuir probe I-V trace with identified plasma potential shown in red (b) Example of RPA probe trace along with IEDF and Gaussian fit

current, the ion energy distribution function (IEDF) can be determined. In our testing, we used a three-grid RPA. The first grid is left floating to minimize perturbations to the plasma. The second grid is biased to a constant -280 V to repel electrons. Compared to the bias voltages required in probing of other EP devices, the magnitude of this electron repelling voltage is nearly 250 V larger.[29] This bias is necessary in ECR thrusters to repel the hot electrons that persist in the far-field plume.[30] For repelling voltages below this threshold, we found that the final current of the RPA trace was negative, suggesting collection of high energy electrons that overcome the second grid's repelling potential. The third grid is the ion-retarding grid, which is swept to high positive voltage. The exact range of the retarding sweep is adjusted depending on thruster power; however, in all cases the maximum retarding potential is high enough that the collected current approaches zero.

The RPA measures energies of the ions relative to ground. However, even in the far field, the plasma maintains some potential above ground. Therefore, it is necessary to correct the ion energies measured by the RPA to account for the plasma potential. To do so, we subtract the plasma potential from the measured probe bias. This correction references ion energies relative to ambient plasma potential rather than ground of the facility. Next, to convert the raw I-V RPA trace into an IEDF we take the derivative, $-\frac{dI}{dV}$. Finally, we fit a Gaussian to the IEDF and extract the mean ion energy, E_i. We show this analysis process in Fig. 9.

3. Faraday Probe

To determine spatially resolved current density, we use a guarded Faraday probe. FP geometry consists of two concentric circular electrodes that area each biased negatively to repel electrons. The outer electrode, referred to as the guard, serves to maintain a flat sheath. This ensures a constant current collection area for the center conductor, the collector. Compared to other EP devices, ECR thrusters present unique challenges for Faraday probing.[9,23,30] According to best practices,[31] the outer diameter of the guard, r_G, should be greater than 50 times the Debye length, $r_G > 50\lambda_D$, to maintain a constant collector area. Given our estimates for $\lambda_D \approx 0.5mm$, this suggests a guard diameter on the order of 5 cm. Furthermore, preliminary testing showed that the probe did not reach ion saturation until biases in excess of -250 V were applied to the guard and collector. Similar to the electron repelling grid of the RPA, this bias is necessary to completely exclude the high temperature electrons present in the plume of the ECR thruster.

With these challenges in mind, we manufactured a custom FP for this work. Following the design of Peterschmitt,[23] the guard has an outer diameter of 5 cm with a 6.35 mm diameter collector at the center. The gap distance between the guard and collector is 0.5 mm. All components of the probe are made from graphite, which was chosen for its low SEE coefficient and its wide availability. The probe is mounted on an optical post and placed 30 mm downstream of the thruster exit. The FP arm is then swept in a semicircular

path across the thruster face using a rotation stage. For all traces the probe bias was held constant at -300 V.

We plot a Faraday probe trace in Fig. 10. We see that the trace generally takes the expected Gaussian current distribution. However, near thruster centerline there is a slight asymmetry in the ion current. This feature has been observed in other FP traces of coaxial ECR thrusters.[23] Although not fully explained, it has been suggested that this asymmetry may arise from the FP interacting with high energy electrons from the antenna[32]. It is also possible that non-uniformity in neutral flow contributes to this asymmetric shape. This artifact has been shown to be more pronounced for radial injection schemes, like the one used in this work, compared to axial injection. Despite the undetermined nature of the asymmetry, this feature was repeatable and consistent, suggesting it does represent a physical feature of the far-field ion current.

By integrating the current density, $j(\theta) = \frac{I_{probe}(\theta)}{A_{probe}}$, of the probe as a function of angular position, θ, and assuming azimuthal symmetry, we recover the total ion current, I_{tot} (necessary for evaluating the efficiency modes as described in Sec. III) according to

$$I_{tot} = 2\pi R^2 \int_0^{\pi/2} j(\theta)\sin(\theta)d\theta, \tag{7}$$

where R is the arm length of the fixture used to sweep the FP. This integral provides the total amount of ion current emitted by the thruster. However, as discussed in Sec. III, only the axial component of ion current contributes to thrust. From our FP sweep, this axial current is determined as

$$I_{ax} = 2\pi R^2 \int_0^{\pi/2} j(\theta)\sin(\theta)\cos(\theta)d\theta. \tag{8}$$

This measurement of axially-directed ion current is complicated by the fact that the background pressure in the vacuum chamber is finite. As high-energy ions near the periphery of the thruster plume interact with the background neutrals, charge exchange may occur. This interaction corrupts the "wings" of the FP trace, resulting in an underestimation of divergence efficiency.[33] To correct for this, we utilize two methods. The first is a flat subtraction, where the minimum value of the current trace is subtracted from the entire current measurement. The second correction is to fit a Gaussian function to our raw FP trace. The ion current of both the flat subtraction and Gaussian fit methods are calculated according to Eq. 8 and the values are used to evaluate uncertainty on our ion current measurements.

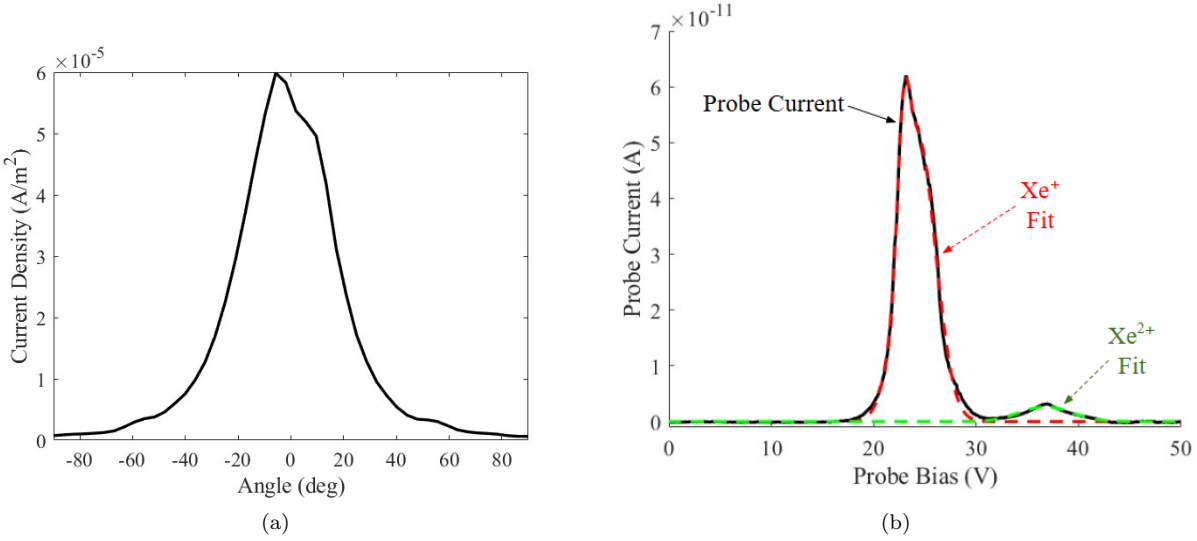

Figure 10. (a) Example Faraday probe trace (b) I-V trace of the ExB probe with examples of fits to the Xe^+ and Xe^{2+} populations

4. ExB Probe

An ExB probe essentially acts as a velocity filter for incoming ions. This probe uses a strong magnetic field, B, perpendicular to a strong electric field, E, to induce a drift in the plasma:

$$v_{ExB} = qE + q(u_i \times B).$$

Only in cases where the ion velocity, u_i, balances the ExB drift velocity, $v_{ExB} = 0 \rightarrow u_i = \frac{E}{B}$, will the ions be able to pass through the probe and reach the collector. Ions with velocities that do not match the drift velocity will be deflected into the walls of the probe. By sweeping voltage on the parallel plates that establish the probe's E field, it is possible to filter over a wide range of velocities. Finally, assuming that all ions undergo a constant potential drop in the acceleration region of the magnetic nozzle (i.e. that the ambipolar field is constant for all ions), an ion's velocity will be directly proportional to its charge state. In this way, we are able to differentiate between charge states of the ion population in the thruster plume.

The ExB probe we used has a B field strength of approximately 1600 G furnished by permanent magnets. The distance between charged plates that establish the E field is 10 mm. The probe is placed 50 cm downstream and traces are taken along thruster centerline. We sweep voltage between the plates from 0 V to 50 V using a Keithley 6482 dual channel source meter. This device also has a channel to read an isolated current from the probe collector.

We analyze the traces of the ExB probe utilizing a Gaussian fit technique outlined by Huang and Shastry.[34] Using this method, Gaussian functions are fit to each charge population and the fit functions, ω, are then integrated and the current fractions for each charge state, Ω_i, are calculated as

$$\Omega_n = \frac{\int_0^{V_{max}} \omega_n(V)dV}{\Sigma_n \int_0^{V_{max}} \omega_n(V)dV}.$$

We found the best agreement when utilizing a bimodal Gaussian function to fit the singly charged population and a unimodal function for the remaining species. We show an example of a probe I-V trace in Fig. 10 along with the Gaussian fits to the charge states.

E. Test Methodology

Challenges with repeatability of results have previously been identified for ECR thrusters,[23] and indeed in the early stages of this work we found wide variability in our performance measurements. In an attempt to improve repeatability and reliability of our measurements, we developed a consistent test methodology. Prior to testing variations to the radial wall and backplate, we treated each material with 1200 grit sandpaper. This was done to both control for surface roughness and remove unwanted contaminant layers such as oxides. Because the anodized oxide layer was part of the study of thruster body material, we did not sand this component prior to testing. Another key point of concern was material outgassing, since boron nitride and aluminum oxide can absorb water from the atmosphere prior to testing. As an initial mitigation strategy, we kept the thruster under vacuum overnight before each test. Furthermore, prior to collecting any data, we operated the thruster at 30 W until a thermal quasi-steady state was achieved. Generally this required approximately two hours of continuous operation. Once thermal quasi-steady state was achieved, we collected all necessary probe data and global performance measurements. Additionally, we took each probe trace three times to evaluate variability in the measurements. Using this testing methodology, repeatability of the data improved to a point where thrust measurements differed by as little as 5% across two test campaigns with the same thruster configuration.

V. Results

In this section, we present the results of our experimental characterization of the thruster configurations described in Sec. IV. We begin by discussing global performance metrics, followed by representative probe data for the baseline configuration. We then examine the agreement between the efficiencies calculated from our direct thrust measurements and far-field probe analysis. We then show global performance measurements and the efficiency breakdowns for the configuration studies.

A. Baseline Configuration Results

We begin this section by presenting the relevant global performance metrics for the baseline configuration. We then show our far-field probe results for the baseline thruster configuration. Although the probe data collected for the various thruster configurations tested in this work vary numerically, the traces remain qualitatively similar. We use these baseline results to point to trends in the data and evaluate agreement between the probes and global performance metrics.

1. Global Performance Metrics

Figure 11 plots floating potential, thrust, specific impulse, and total efficiency for the baseline thruster configuration. The data presented in Fig. 11 represents a combination of data across two different test campaigns several weeks apart. We analyze uncertainty in these metrics following the framework outlined by Wachs.[6]

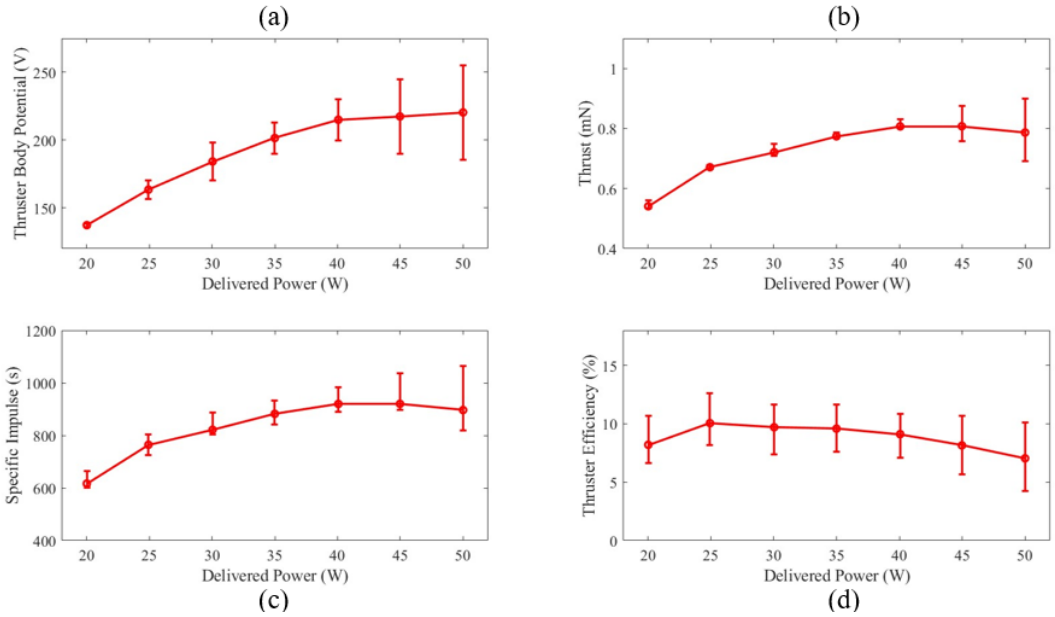

Figure 11. (a) Body floating potential (b) Thrust (c) Specific Impulse and (d) efficiency for the baseline thurster configuration

We see from this plot that thrust, specific impulse and floating potential all increase with power. Over the range of powers tested, floating potential increases from approximately 140 V to 220 V. Because the body is electrically tied to the radial walls of the plasma source region in the baseline configuration, higher thruster floating voltage is indicative of higher plasma potentials in the source region. This is an expected trend, since higher delivered power corresponds to more power coupled into the plasma. Thrust increases from 0.55 mN to 0.78 mN and specific impulse increases from nearly 600 s to just under 900 s. The final performance metric that we comment on is total efficiency. We first see that efficiency of the device is between 5-10%. We also note that the uncertainty in total efficiency is higher than the other metrics. This is primarily due to the uncertainty on microwave power delivered to the thruster, which is approximately 10% in our experimental setup. We find that efficiency appears to peak between 25-30 W and then decreases at higher powers. The presence of this optimal operating condition has previously been observed in literature,[9] and was attributed to opposing physical trends as a function of power. It was shown that as power increases, ionization fraction improves, but wall losses become worse. The optimal operating condition balances these effects, resulting in a peak in total efficiency. We continue the discussion of scaling of the plasma properties as a function of power in the following subsections.

2. Plasma Properties

Figure 12 shows plots of the plasma potential and electron temperature in the baseline configuration as a function of delivered power to the thruster.

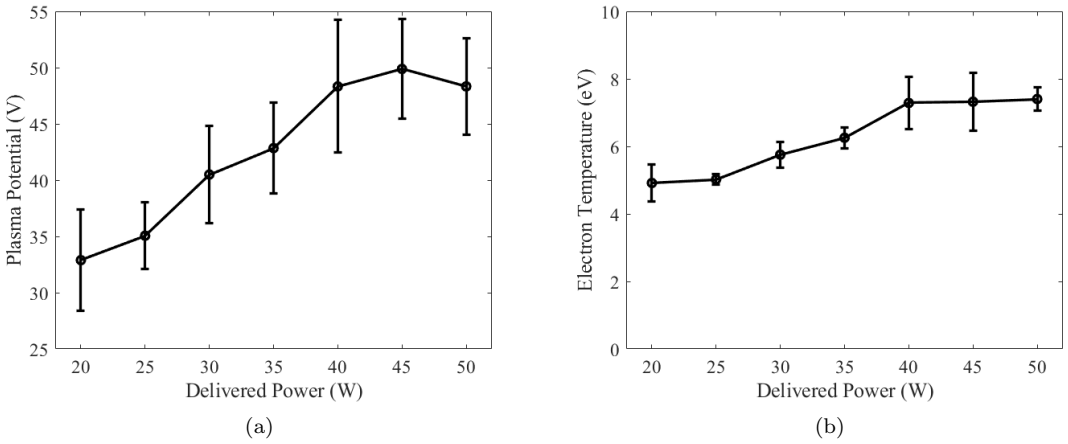

Figure 12. (a) Calculated plasma potential and (b) electron temperature as a function of power

The first trend shows that as delivered power increases, the far-field plasma potential rises. This may be indicative of increasing potentials in the source region with power. This observation agrees with the baseline floating potential measurements, which also suggest a direct relationship between power and plasma potential in the source. We also comment on the uncertainty in this measurement. As discussed in Sec. IV, for each operating power we take three LP traces and use three different methods to determine plasma potential. Error bars represent 2σ of these calculations, capturing our 95% confidence interval.

Similarly, as shown in Fig. 12(b), electron temperature in the far-field also increases with absorbed power. However, we note that the far-field electron temperatures are only between 5-10 eV and the difference in temperature between 20 W to 50 W is only 2-3 eV. These moderate values are likely an order of magnitude smaller than the estimated temperatures in the source region.[26,35,36] This is a reflection of the fact that far-field measurements are downstream of where the magnetic nozzle has served to convert the majority electron thermal energy into ion kinetic energy.

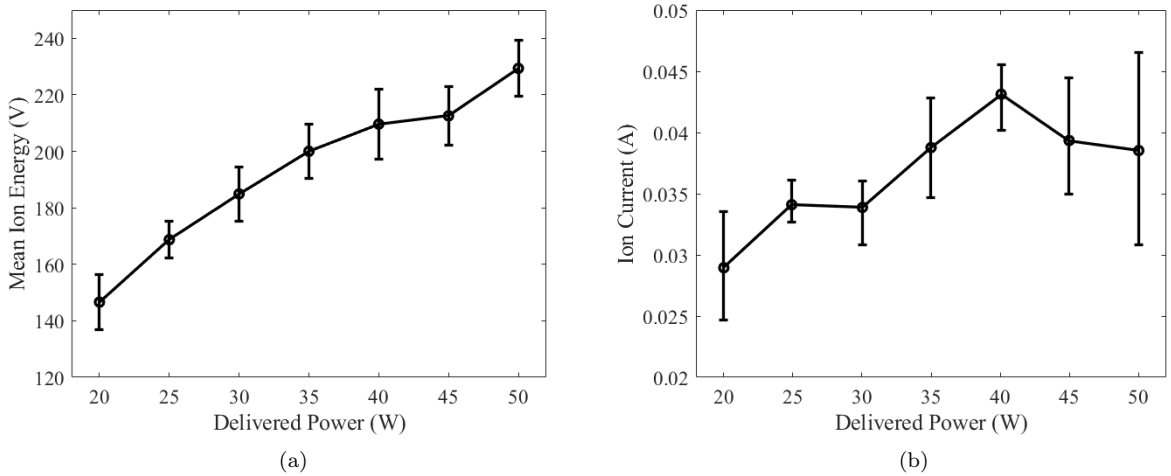

Figure 13. (a) Mean ion energy and (b) Total ion current as a function of thruster delivered power

Figure 13(a) shows the mean ion energy as a function of power. These values have been corrected for the plasma potential, meaning that the uncertainty from Fig. 12 propagates to this measurement with additional error arising from the Gaussian fit to the IEDF. Even beyond uncertainty, we see that ion energy increases

monotonically with delivered power. Physically, this trend arises from the fact that more energy is deposited into the electrons, i.e. higher electron temperatures in the source region (see Fig. 12(b)). In turn, these enhanced electron temperatures result in stronger ambipolar accelerating fields, yielding an increased mean ion energy.

Figure 13(b) shows the total ion current, calculated according to eq. 7, as a function of power. The uncertainty in this metric arises from the repeatability of the FP trace, which was repeated three times. This plot highlights the general trend that ion current increases with power. This increase can largely be explained by considering the effect of delivered power on electron temperature. As shown in Fig. 12, higher powers correspond to higher electron temperatures. These higher electron temperatures increase the ionization rate within the source region, increasing the ion current measured by the far-field FP.

Finally, we comment here on the results of the ExB measurements, as shown in Fig. 10. In agreement with previous ExB measurements for low-power ECR devices, we find that the plume is primarily comprised of singly charged ions when the thruster is operating on xenon [7]. We observe 90%-95% singly charged current fraction and do not see a detectable charge state above Xe^{2+}. Additionally, we find that the current fractions remain approximately constant as a function of power.

3. Efficiency Modes

Leveraging the probe data discussed in the previous subsection, we show in Fig. 14 the efficiency modes as a function of power. We also include a comparison between the total efficiencies derived from plasma properties and direct thrust measurements.

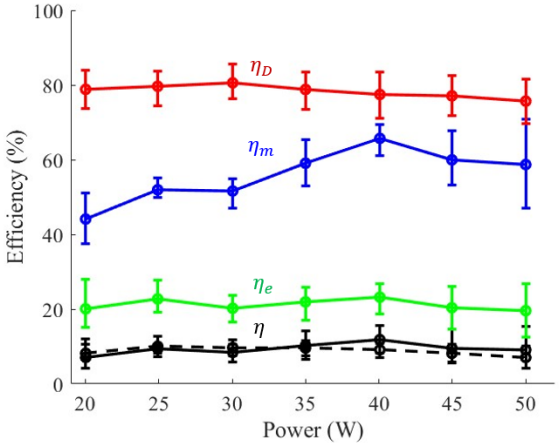

Figure 14. Efficiency modes as a function of power for the baseline thruster configuration operating at 1 SCCM-Xe. Total efficiency determined from direct thrust measurements (dashed) compared to plasma diagnostics (solid)

We first comment on the relative values of the efficiency modes and their trends with power. Divergence efficiency is the highest mode, ranging from 70% to 80%. Although the average value decreases by approximately 4% as power increases, when accounting for uncertainty arising from variability in our measurement and background subtraction technique, we do not find strong scaling with divergence efficiency as a function of power. This result is expected, as divergence efficiency is most likely dominated by the magnetic field shape and the location where the plasma detaches. A relatively constant divergence efficiency suggests that these physical processes are largely unaffected by changes in thruster power.

The next highest efficiency mode is mass utilization, ranging from approximately 45% to 65%. This range of values agrees with previously published efficiency analyses for ECR thrusters operating at this power class.[9,37] Commensurate with the previously noted trend in ion current, we find that mass utilization tends to increase with delivered thruster power. As with ion current, the physical explanation for this trend is the higher ionization rate resulting from elevated electron temperatures in the source region when power increases.

The lowest of the three efficiency modes is energy efficiency. This term ranges values from 18% to 25% for the baseline configuration. We do not observe strong scaling with power outside of the uncertainty caused

by variability in our plasma potential, RPA measurements, ion current measurements, and thruster power. However, the average energy efficiency measurement appears to reduce by approximately 5% in the tested power range. This is an interesting result given that we previously found that both ion current and mean ion energy increase as a function of power. Examining eq. 6, we would expect energy efficiency to follow a similar trend. The physical intuition that can be derived is that, although ion current and ion energy increase, they do so less dramatically than the power delivered to the thruster. This suggests that for higher input powers, a larger fraction of that delivered power is lost, despite the fact that there is indeed more total power deposited into the ions. The higher losses at higher power has been suspected to result from increased wall losses.[9] The physical cause of this high power loss to the wall may again be attributed to increased electron temperatures in the source. The corresponding increase in electron mobility results in higher plasma densities near the wall, which yields higher losses. We return to this point in Sec. VI.

Finally, the product of these three efficiency modes yields a calculation of total thruster efficiency. This property, derived from probe measurements, is the same as the global performance metric discussed in the previous section. This allows us to compare the efficiencies measured by two independent techniques. In Fig. 14, we show the efficiency calculated from the efficiency mode analysis as a solid black line and compare that to the efficiency determined from direct thrust measurements. From this comparison, we find good agreement between the two total efficiency calculations. At all powers tested, the two methods agree within uncertainty. This lends credibility to our probe measurements and serves as validation that our far-field probe suite accurately captures the physical behavior of the thruster.

B. Radial Wall Material Results

In this section we present the results of our of radial wall material study. We begin with global performance, determined by direct thrust measurements and the supporting thruster infrastructure. We then compare the efficiency modes for each material as a function of power. For each material, propellant flow rate is held constant at 1 SCCM-Xe. Power is controlled to the desired setpoint using a PID control loop that receives real-time feedback from the power measurement equipment described in Sec. IV.

1. Global Performance Metrics

We present in Fig. 15 the body floating potential, thrust, specific impulse, and total efficiency for the UM ECR VII thruster operating with four different wall materials.

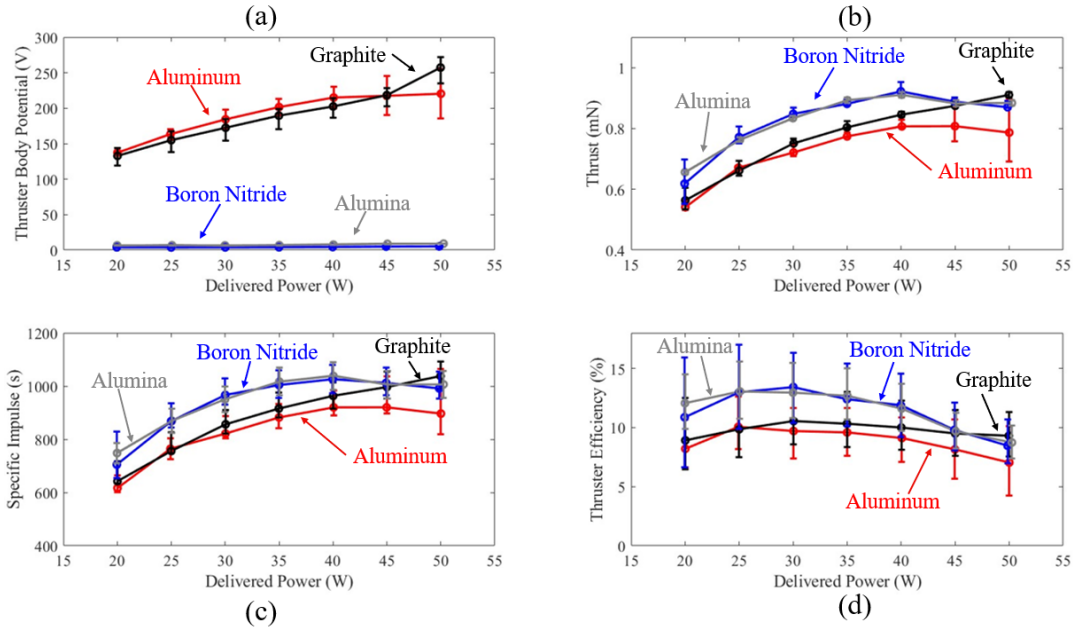

Figure 15. Global performance metrics measured at 1 SCCM-Xe for each radial wall material a) body floating potential b) thrust c) specific impulse d) total efficiency.

One immediate difference highlighted in Fig. 15(a) is the 150 V-250 V change in thruster floating potential depending on the electrical conductivity of the material used. This difference arises because the insulating radial wall material isolates the thruster body from the plasma potential within the source region. We continue discussion of body floating potential and other effects of wall conductivity in Sec. VI.

Next, we see that for the majority of power levels tested in this investigation, boron nitride and alumina outperform the other materials. Fig.15(b), (c) and (d) show that from 20-40 W, the thrust, specific impulse and total efficiency are higher for boron nitride and alumina than graphite and aluminum. These results afree with previously reported performance comparisons between conducting and insulating materials[9,10]. However, at 45 W and 50 W the performance of alumina, boron nitride and aluminum decrease, while graphite does not exhibit this performance decrease. As a result, at the 45 and 50 W power condition, graphite, alumina, and boron nitride exhibit comparable performance. We discuss potential physical explanations for these trends in Sec. VI.

2. *Efficiency Modes*

In this subsection we present the efficiency modes of the thruster as a function of power for each thruster wall material tested. Fig. 16 compares the three efficiency modes for each material. An error in our experimental setup prevented us from performing a full efficiency mode characterization of the alumina test article. However, given the nearly identical global performance to BN, we expect the efficiency modes between alumina and boron nitride to be very similar as well.

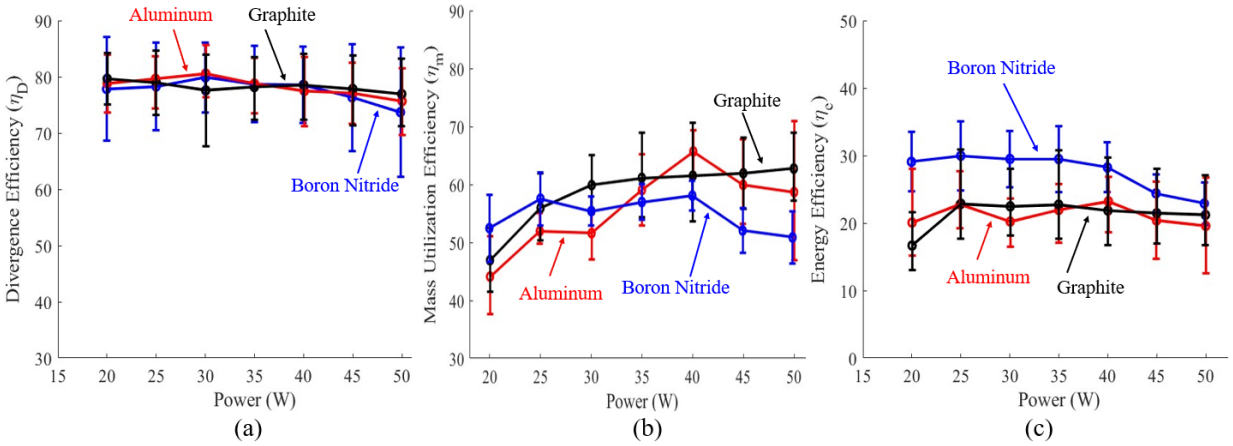

Figure 16. (a)Divergence Efficiency (b)Mass Utilization Efficiency (c) Energy Efficiency as a function of power for the radial wall materials tested at 1 SCCM-Xe

From these efficiency modes, we can gain more physical insight into the global performance data presented in the previous section. Beginning with divergence efficiency, plotted in Fig. 16 (a), we note that all materials exhibit a weak trend of decreasing average divergence efficiency as power increases. This is consistent with the trend found for the baseline configuration. Across materials, the divergence efficiencies are within error. Physically, this is likely a reflection of the fact that divergence is dominated by the field topology of the magnetic nozzle, which remains constant across all configurations tested.

Next, we examine mass utilization efficiency, which is plotted in Fig. 16(b). Here we see that aluminum and graphite match the baseline trend of increasing mass utilization as a function of power. However, boron nitride does not. Instead, the mass utilization of the thruster equipped with BN walls appears to remain relatively constant between 20 W to 40 W and then decreases at higher powers. This decrease in mass utilization is further investigated in Sec. VI. However, we note here that at powers above 30 W, boron nitride has the lowest mass utilization of the materials tested. Therefore, an argument relating to improved mass utilization does not explain the improved performance for BN radial walls.

Finally, Fig. 16(c) shows the energy efficiencies of the tested materials as a function of power. Immediately we notice that the energy efficiency for boron nitride walls is nearly 10% higher than the other materials tested. This points to higher energy efficiency as the cause of the increased overall performance for the BN radial wall configuration. We expand on the underlying physical processes of this result in Sec. VI. We

also note that each material shows a slight decrease in the energy efficiency mode as power increases. This trend is especially notable for the BN wall, which demonstrates a nearly 10% reduction in energy efficiency between 40 W and 50 W.

For all radial wall materials tested in this effort, energy efficiency is the lowest efficiency mode measured. Commensurate with previous probe analyses of ECR thrusters,[7,9,23,38] this suggests that poor conversion of microwave power into ion kinetic power is the primary limitation to overall efficiency of the device. Although this study has demonstrated that the radial wall configuration can increase energy efficiency, even for the highest performing material, energy efficiency is only improved by 10% and total efficiency increases from approximately 10% in the baseline, to 13%. This suggests that choice of radial wall material alone is likely insufficient to substantially improve overall performance of the device. In the following sections, we continue our study of wall material effects, focusing on other components of the thruster to better understand where these loss mechanisms occur.

C. Backplate Material Results

Here we present the results from our investigation of varying backplate material. As with our radial wall study, we collect all data at a flow rate of 1 SCCM-Xe and delivered powers ranging from 20 W to 50 W.

1. *Global Performance*

Figure 17 shows the floating potential, thrust, specific impulse, and total efficiencies of the two backplate materials studied. Each backplate configuration is equipped with the anodized thruster body, and aluminum radial walls. Note that the BN backplate configuration is the baseline case, which has been plotted here to allow for direct comparison.

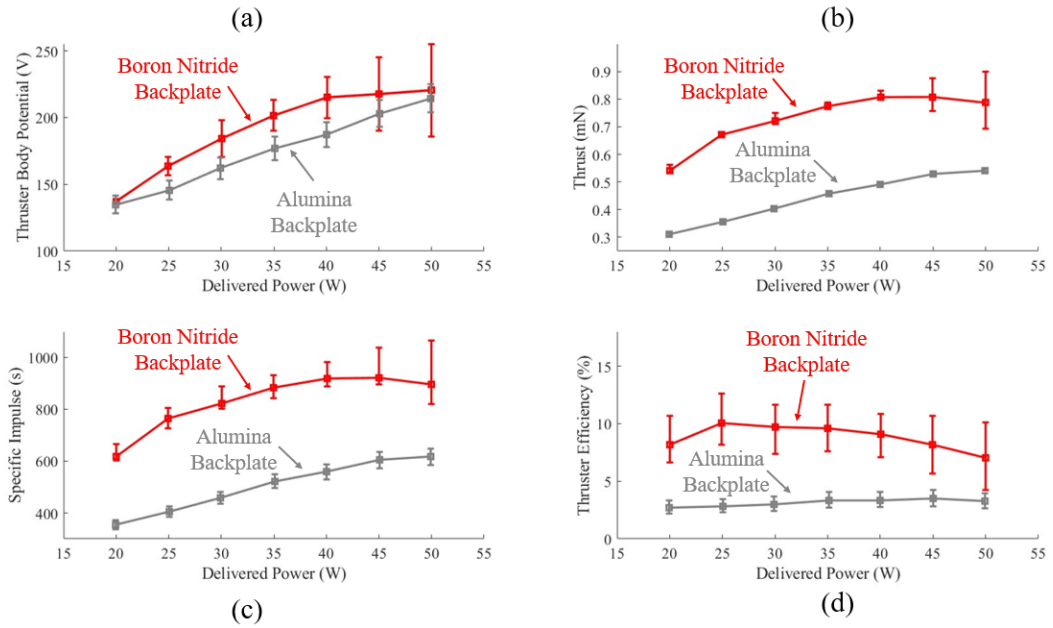

Figure 17. Comparison of (a) body floating potential (b) thrust (c) specific impulse (d) total efficiency between alumina and boron nitride backplate materials

Qualitatively, the alumina backplate performs worse in every key performance metric. Thrust and specific impulse decrease by over 50% and total efficiencies are approximately 1/3 of the baseline configuration. Interestingly, the floating potential for the alumina backplate is also lower than the BN baseline. This is a departure from the trend observed in our radial wall material testing, where lower floating potential did not necessarily correspond to decreased performance. We further discuss the physical implications of these floating potential measurements in Sec. VI.

2. *Efficiency Modes*

To gain insight into the physical reason for the decreased performance of the alumina backplate, we next examine the efficiency modes measured with the alumina backplate and compare them to the baseline configuration. This comparison is made in Fig. 18

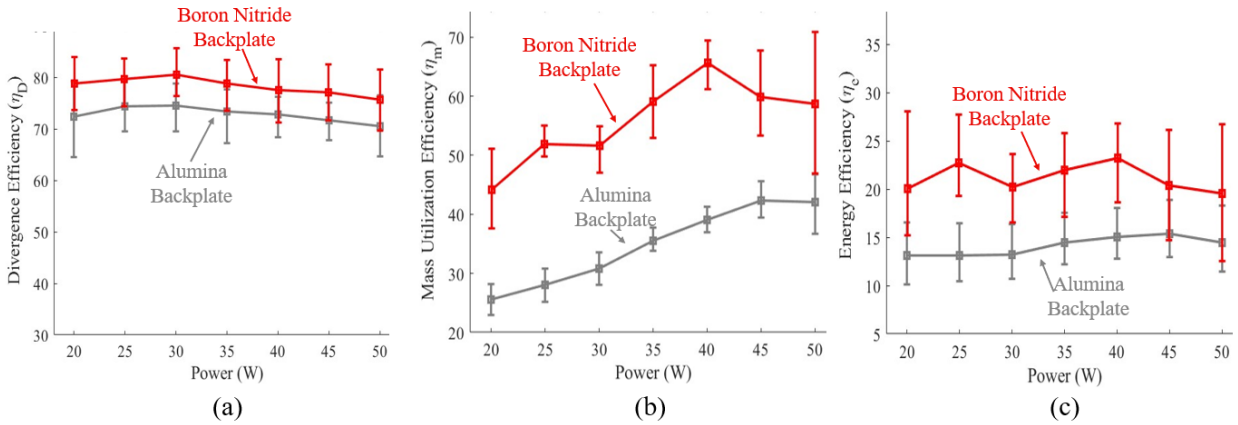

Figure 18. (a) Divergence Efficiency (b) Mass Utilization Efficiency (c) Energy Efficiency as a function of power for the backplate materials tested at 1 SCCM-Xe

Our first observation of efficiency modes in the backplate material study concerns divergence efficiency. Although the average divergence efficiency measurement decreases by approximately 5% for the alumina backplate, this is within error of the divergence efficiency for the baseline configuration. This again seems to suggest that plume divergence is relatively insensitive to changes in source region configuration.

Analyzing the next efficiency mode, mass utilization efficiency, we see that the alumina backplate yields lower performance. Mass utilization for the alumina backplate configuration is decreased by as much as 25% compared to BN. However, the trend of increasing mass utilization as a function of power persists across both backplate configurations. This is an interesting result, as we generally expect power loss terms to dominate at higher powers. We expand upon this discussion in Sec. VI.

Finally, energy efficiency of the alumina backplate is measured to be 30% lower than the baseline configuration. That said, we again find a departure from the power scaling observed for the baseline configuration. Rather than a slight decrease, the alumina backplate exhibits an increase of approximately 5% in average energy efficiency as power increases. This again points to unique scaling of power losses to the backplate compared to the loss mechanisms to the radial wall. Combined with the poor mass utilization efficiency, these decreased energy efficiency suggest that the alumina backplate configuration causes increased power losses in the system. These higher power losses ultimately contribute to the lower measured global performance.

D. Thruster Body Material Results

In this section we present the results of the final material study, this time changing the configuration of the thruster body. As with the previous studies, all data we present is collected at 1 SCCM-Xe.

1. *Global Performance*

Figure 19 compares the global performance metrics between the two thruster body materials. We find from these plots that the untreated thruster body drives down performance of the thruster. Floating potential is lowered by approximately 80 V at all powers. Thrust and specific impulse decreases by over 40%, while efficiency drops by as much as 75% compared to the baseline anodized body. Interestingly, we also observed changes in performance trends between the two body materials. Although floating potential increases monotonically with power for the untreated body, the floating voltage only increases by 40 V over the power range tested. This is lower than the 85 V increase observed in the baseline case. Furthermore, thrust and specific impulse hardly increase at all over the 20 W to 50 W testing window. In both cases the trend is nearly flat,

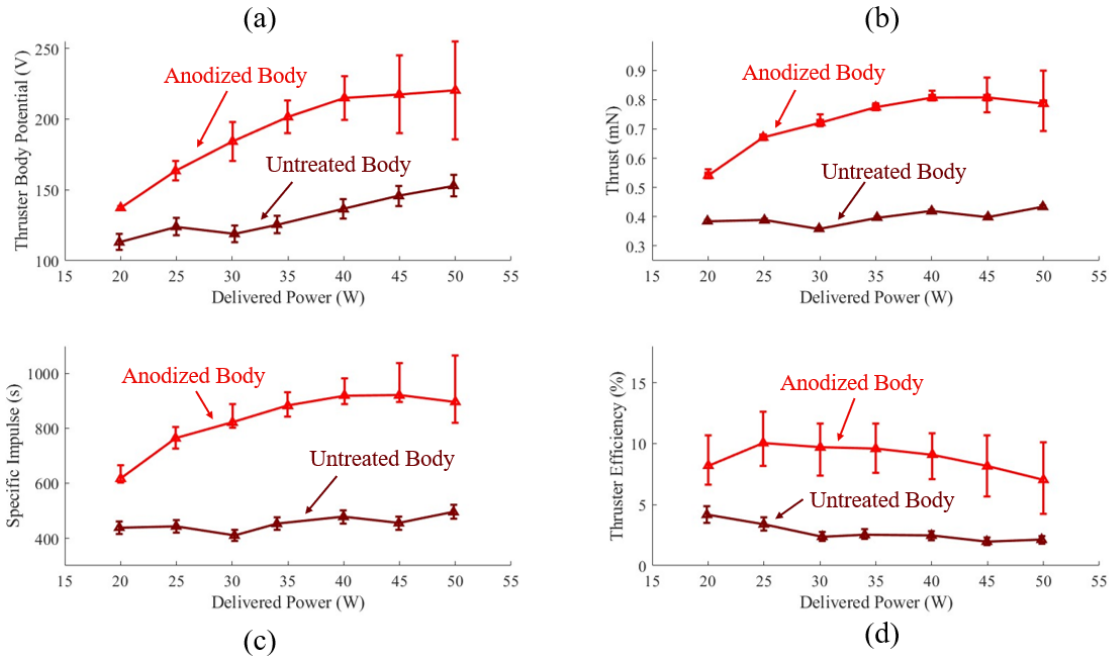

Figure 19. Comparison of (a) body floating potential (b) thrust (c) specific impulse (d) total efficiency between the anodized and untreated thruster body

only increasing by approximately 10% between the 20 W and 50 W operating conditions. Finally, for total efficiency, we see that it decreases monotonically with power. This is a departure from the typical trend of efficiency peaking at 25 W-30 W, as observed in the baseline case. To better understand the physical reasoning for these results, we next compare the efficiency modes between the two thruster body materials.

2. *Efficiency Modes*

Here we compare the efficiency modes calculated by the far-field probes for both thruster body materials. Unfortunately, during the 30 W FP sweep, a large arc damaged the power delivery cable to the thruster. This prevented us from completing the efficiency mode analysis beyond 30 W. Therefore, we limit the comparison of efficiencies to 20 W - 30 W. Examining the efficiency modes presented in Fig. 20, we first find that

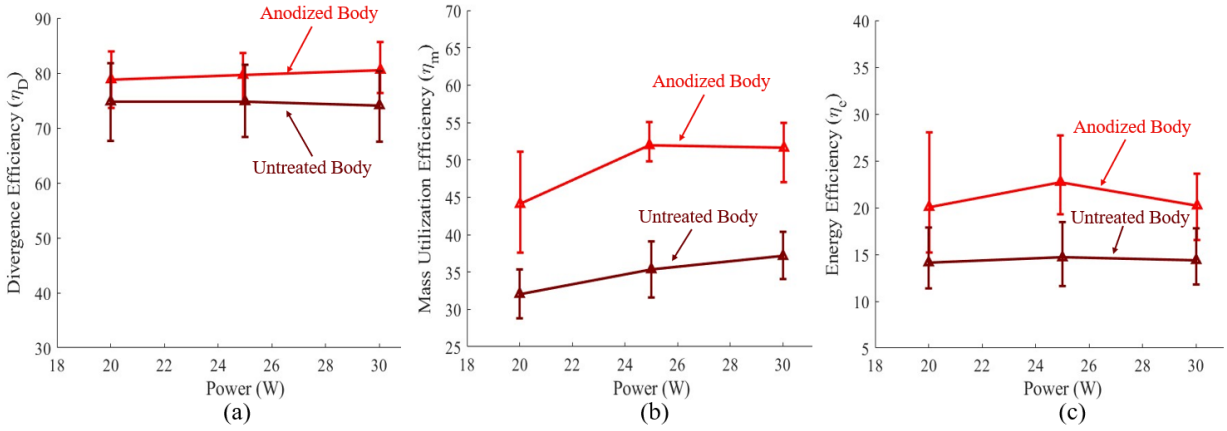

Figure 20. (a) Divergence Efficiency (b) Mass Utilization Efficiency (c) Energy Efficiency as a function of power for the thruster body materials tested at 1 SCCM-Xe

divergence efficiencies fall within uncertainty between the two materials. Although the average value of the

untreated body divergence is slightly lower than the baseline case, this discrepancy does not explain the difference in total performance. Instead, the second efficiency mode, mass utilization, is likely the main driver in lower total performance for the untreated body. We see from Fig. 20(b) that both mass utilization efficiencies follow a similar increasing trend in power, but this mode is 25% lower for the untreated body compared to the baseline. Energy efficiency is also lower for the untreated body by nearly 30%. Therefore, the decrease in global performance resulting from the untreated thruster body appears to be a combination of decreased mass utilization and energy efficiency. We provide additional physical insight as to why the untreated body lowers these efficiency modes in Sec. VI.

VI. Discussion

In this section we first quantify the previously discussed hypotheses relating to wall conductivity and SEE. We then examine the results of the studies presented in the previous section and evaluate the agreement between the proposed physical effects and our experimental data.

A. Effects of Wall Conductivity

We have qualitatively described the effects of wall conductivity in Sec. II. Fundamentally, this hypothesis relates to loss currents within the plasma. In the next section we formulate a current balance model that can be used to evaluate these loss currents.

1. Current Balance Loss Model

As discussed in Sec. II, the walls must maintain a zero net current condition. To satisfy this condition, a potential drop forms at the interface between the plasma and the wall. We can then model the ion and electron loss currents to the walls, I_{iw} and I_{ew}, using the solutions for plasma current into a sheath. These currents take the form

$$I_{iw} = -\exp\left(-\frac{1}{2}\right) q n_0 A_w \sqrt{\frac{qT_e}{m_i}}, \tag{9}$$

$$I_{ew} = q n_0 A_w \sqrt{\frac{qT_e}{2\pi m_e}} \exp\left(\frac{V_f - V_p}{T_e}\right). \tag{10}$$

In the above equations, we have defined n_0 as the assumed plasma density in the source, m_e is the electron mass, V_f is the floating potential of the wall, V_p is the plasma potential in the source, and A_w is the surface area of the wall. In the case where the walls are non-conducting, the zero current requirement mandates that $I_{iw} = I_{ew}$. However, in the case where the walls are electrically conductive, this simplified loss circuit extends to include the thruster body. In this case, additional current may be lost to the body of the thruster and must be included in the overall current balance. These losses are described by

$$I_{ib} = -\exp\left(-\frac{1}{2}\right) q n_{noz} A_b \sqrt{\frac{qT_{e_{noz}}}{m_i}}, \tag{11}$$

$$I_{eb} = q n_{noz} A_b \sqrt{\frac{qT_{e_{noz}}}{2\pi m_e}} \exp\left(\frac{V_f - V_{p_{noz}}}{T_{e_{noz}}}\right). \tag{12}$$

These expressions take the same form as the losses in the source region with a few differences. First, the loss surface is the area of the body, A_b. Second, the thruster body is interacting with the plasma downstream of the source, where the local plasma properties, such as electron temperature, density, and plasma potential, are different. We denote this difference using the *noz* subscript.

When considering losses to all conducting surfaces, the zero net current condition becomes

$$I_{iw} + I_{ib} = I_{ew} + I_{eb}. \tag{13}$$

This current balance requirement, combined with the expressions for ion and electron loss currents allow us to examine the behavior of loss mechanisms in the thruster when the conductivity of the components are changed.

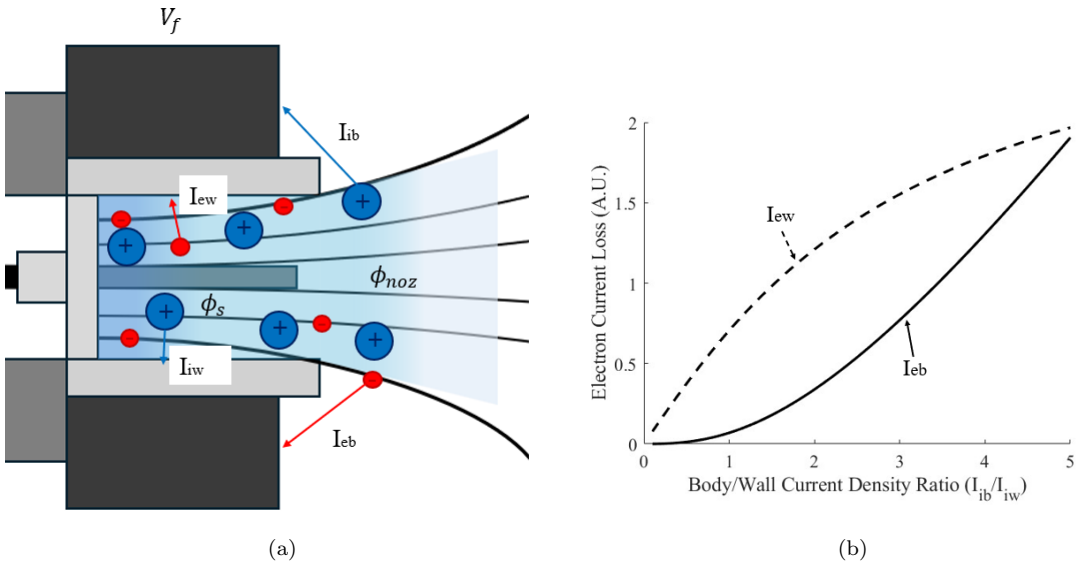

(a) (b)

Figure 21. (a) Diagram of current losses to the source region walls and thruster body (b) Scaling of electron loss currents to the radial wall and thruster body as a function of ion current ratio

We begin by parameterizing the losses in terms of the ion current ratio between the source region wall and thruster body, $\frac{I_{ib}}{I_{iw}}$. We next assume values for several plasma properties. First, we assume that the electrons in the source region have a temperature of 50 eV and a plasma potential of 300 V. These estimates are informed by results of computational models for ECR thrusters.[35] Second, in the downstream region, near the body, we assume electrons have cooled to 30 eV and the local plasma potential has dropped to 250 V. This electron cooling and potential drop both result from the dynamics of the magnetic nozzle, where electrons lose thermal energy and plasma potential drops.[39] With these assumptions, we can solve eq. 13 for thruster floating potential and subsequently examine the behavior of the electron loss currents. We show the results in Fig. 21

First, we provide context for the ion current density ratio that we use in our model. Low ratios of ion body current to ion wall current correspond to the case of insulating radial walls, where the body is not electrically connected to the loss circuit and therefore is assumed to collect no current. Conversely, high ratios of ion body to wall current represent cases like the conductive body test, where a majority of current density can be collected by the body due to its increased conducting area. With this in mind, we see that increasing the amount of current collected by the body increases electron losses to both the body and the radial walls of the source. This result makes intuitive sense, as increasing the ion current collected by the body corresponds to an increase in the area of the thruster exposed to the plasma. We also note that for low ratios of $\frac{I_{ib}}{I_{iw}}$ the electron losses are primarily dominated by the radial wall. However, as the ratio of ion current increases, the electron losses to the body grow exponentially and become a significant loss mechanism. Later in this subsection, we evaluate the implications of this scaling on our experimental results.

B. Effects of Wall Secondary Electron Emission

As described in Sec. II, two competing phenomena have been qualitatively proposed to explain the relationship between wall SEE and plasma behavior in ECR thrusters. In the remainder of this subsection, we discuss the scaling of these effects.

1. Hypothesis 1: Secondary Electrons Replenish Lost Primaries

Typically, electrons lost to the walls of the plasma source represent an irrecoverable loss mechanism. However, for wall materials with high SEE, loss of the primary electrons to the walls may be partially offset by the secondaries emitted at the wall. In this case, an additional source term would be added to the steady-state

plasma continuity equation, taking the form

$$\frac{\partial n}{\partial t} = 0 = K_{iz}(T_e) n_e n_n - \frac{D}{A_{source}} n_e \left(1 - \gamma\right). \tag{14}$$

Here $K_{iz}(T_e)$ is the temperature-dependent ionization rate, n_e is the average plasma density, n_n is the average neutral density, D is the cross-field diffusion coefficient, and A_{source} is the cross-sectional area of the source region and γ is the material SEY. We solve eq. 14 numerically, assuming a Bohm-like diffusion coefficient and constant neutral gas density. We show the scaling of ionization rate as a function of SEE in Fig. 22. From this plot we indeed see that under these assumptions, SEE will increase ionization rate. This increase should manifest in our efficiency mode analysis as an increase to mass utilization efficiency.

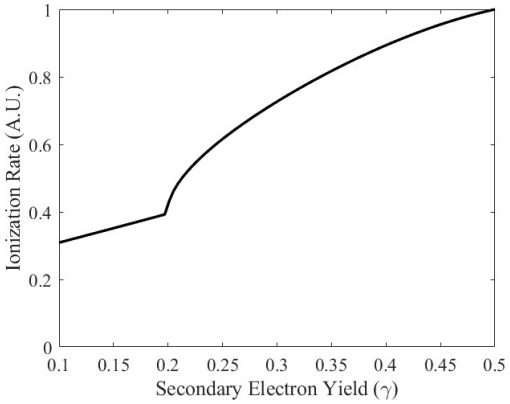

Figure 22. Ionization Rate as a function of Secondary Electron Yield

2. Hypothesis 2: SEE Increases Electron Losses to the Walls

The second effect attributed to SEE is a decrease to the repelling sheath potential. In the presence of SEE, the sheath potential, ϕ_s, is described by[14]

$$\phi_s = T_e \ln\left[(1 - \gamma)\sqrt{\frac{2m_i}{\pi m_e}}\right]. \tag{15}$$

A decrease in the magnitude of this sheath potential drop results in an increase electron current to the wall and therefore an increased power loss. Mathematically, this power loss is related to the sheath potential drop as[15]

$$P_{ew} \propto \exp\left(\frac{\phi_s}{T_e}\right). \tag{16}$$

In Fig. 23, we plot the scaling of power loss to the walls as a function of SEE. This scaling shows that an increase in SEE exponentially increases power losses. We expect these losses to appear in both the mass utilization and the energy efficiency. Mass utilization will likely decrease because of the electron density lost to the wall. Similarly, we expect energy efficiency to drop, as the power that was deposited into the electrons is lost to the walls rather than being converted into ion kinetic energy.

C. Radial Wall Material Study

Examining the results of our radial wall material study we see that the boron nitride and alumina walls generally outperform the other two materials. Graphite is the third highest performing material, with aluminum resulting in the lowest performance. Here we evaluate these trends in the context of the two prevailing hypotheses relating to wall material effects.

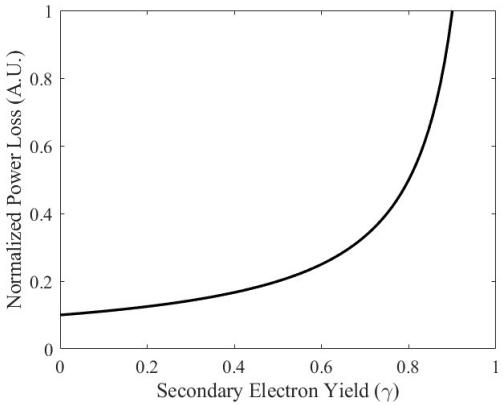

Figure 23. Normalized Power Loss as a function of Secondary Electron Yield

Radial Wall Conductivity Effects

Based on the wall conductivities plotted in Fig. 2, we see that thruster performance is a strong function of material conductivity. Specifically, electrically insulating materials yield improved performance. Furthermore, we find that the body floating potential also correlates directly with the conductivity. This suggests that the conductivity of the radial wall directly impacts the boundary condition between the plasma and the thruster body. When the wall is conductive, the body floats to a potential that is approximately equal to the source plasma potential minus the sheath potential drop at the wall. According to the current loss model presented in Sec. VI.A, this large positive charge (increased V_f) will increase the electron current loss to the body. In this way, we expect configurations with conducting wall materials to increase plasma losses to the walls. Indeed, this may be one explanation for the observation of improved energy efficiency when the radial wall is made of an insulating material.

Radial Wall Secondary Electron Emission

Referencing the secondary electron yield of the radial wall materials tested (see Fig. 3), we indeed find that alumina and boron nitride have higher SEY than graphite and aluminum. Initially, based on the fact that alumina and BN also have the highest global performance, this appears to support the hypothesis that secondaries may replenish lost primary electrons. Furthermore, as shown in 16, at 20-25 W the mass utilization of BN is approximately 5% higher than the other two materials. However, as power increases, the mass utilization of BN remains constant while the other two materials improve. As a result, between 35-50 W BN has the lowest mass utilization of the materials tested. We would expect that these higher powers would lead to more SEE, which should increase mass utilization according to the first hypothesis relating to SEE. Finally, we see that the global performance metrics of the alumina radial wall and BN wall are nearly identical, despite the fact that alumina's SEY is generally about 1.5 times higher than that of BN. This suggests that the conductivity of the materials dominates the overall thruster behavior. Based on these results, we conclude that the improved performance of the alumina and BN radial walls likely does not stem from improved mass utilization resulting from secondary electrons.

The second hypothesis relating to SEE is proposed to cause a decrease in device performance. Though alumina and BN are the best performing material for the majority of the power levels tested, examining Fig. 15, we see that the performance of both materials decreases at powers above 40 W. This observation also extends to aluminum, which has the third highest SEY of materials tested. According to Fig. 12 higher power operation corresponds to elevated electron temperatures. From Fig. 3, we also find that higher electron temperatures increase SEE. As shown in Fig. 23, this elevated SEE will cause an exponential increase in electron loss to the wall. Therefore, we attribute the decrease in performance of the alumina, BN, and aluminum walls at high powers to increased losses resulting from SEE. This finding may suggest that the trends in performance that we observe in this work do not hold at higher delivered powers. As the ratio of thruster delivered power to neutral flow increases, electron temperature will continue to increase, as will the wall SEE. Based on our efficiency mode analysis, we expect that wall losses will also continue to

increase, which will drive down overall thruster performance.

D. Backplate Material Study

The results of our backplate material study show that the alumina backplate results in decreased mass utilization and energy efficiency compared to BN. Here we discuss the physical reasoning for this trend.

Backplate Secondary Electron Emission

Based on Fig. 3, we find that alumina has a higher SEY than BN. However, similar to our findings in the radial wall material study, we again do not see any clear relationship between SEE and mass utilization efficiency. This further refutes the first hypothesis relating to SEE. With that said, the lower energy efficiency and lower mass utilization resulting from the alumina backplate seemingly support the suggestion that SEE increases wall losses.

However, as we examine the behavior of the efficiency modes as a function of power, we see that the losses do not appear to scale. Based on Fig. 23, we would suspect that the power losses resulting from SEE effects should get worse as power increases. This should result in a decrease in the mass utilization and energy efficiency of the alumina backplate at 50 W compared to 20 W. Indeed, this is the trend that we see for the BN radial wall. Instead, both mass utilization and energy efficiency increase as a function of power for the alumina backplate tests. One possible explanation is that the increased SEE of the alumina backplate results in a space charge limited sheath. Once the sheath reaches the space charge limit, the scaling of wall losses become linear with temperature, rather than exponential. This less aggressive scaling may prevent wall losses from dominating at high powers, preserving the baseline trend of increasing mass utilization with increased delivered power. A second possibility is that there are other loss mechanisms arising from material effects that we have not yet considered. In the next subsection we discuss one such physical loss mechanism: dielectric tangent losses.

Backplate Dielectric Strength

Although both backplate materials tested are good electrical insulators, they do have differing dielectric strengths. As shown in Fig. 4, the antenna passes through the backplate of the thruster. This means that in the region between the microwave cable termination and the opening of the plasma source, the backplate itself must serve as a transmission line. Therefore, the dielectric strength of the backplate may affect the amount of microwave power deposited into the plasma.

We can express the power dissipated in a dielectric material as

$$P_{loss} \propto \frac{1}{2}\omega_{RF}|E|^2\epsilon_0\epsilon'\tan\delta, \tag{17}$$

where ω_{RF} is the angular microwave frequency, $|E|$ is the magnitude of the electric field, ϵ_0 is the permittivity of free space, ϵ' is the real component of the material's relative permittivity, and $\tan\delta$ is the material loss tangent. In this work, we hold the microwave frequency constant and assume the power infrastructure delivers a constant electric field magnitude to the backplate. Under these assumptions, the ratio of dissipated power between BN and alumina can be expressed as

$$\frac{P_{loss_{BN}}}{P_{loss_{Alumina}}} \propto \frac{\epsilon'_{BN}\tan\delta_{BN}}{\epsilon'_{Alumina}\tan\delta_{Alumina}} \approx 0.70. \tag{18}$$

We note that these properties depend heavily on the material grade, and we do not have direct data available for the materials used in this work. However, based on commonly reported values in literature,[40–42] we do find that the alumina backplate results in higher power loss than BN. This fact could explain the trends in efficiencies observed in Fig. 18. Indeed, we find that the trends in mass utilization and energy efficiency more closely match the baseline configuration, than the expected scaling with SEE losses.

Finally, we note here that there is an example of an ECR thruster operating with an alumina backplate that we can reference in literature. A waveguide prototype constructed by Peterschmitt utilized alumina as the rear wall of the source region.[16,23] After characterization, it was found that this device produced lower ion current and decreased ion energies compared to the coaxial thruster that utilized a BN backplate. Though this decreased performance was primarily attributed to the difference in coupling scheme, the physical

reasoning for decreased performance shows good agreement with our backplate efficiency mode comparison. Therefore it is possible that a difference in backplate material also contributed to the performance decrease.

E. Thruster Body Material Study

To conclude this section, we discuss the results of our thruster body material investigation. Because the thruster body does not directly interact with the high density, high energy electrons in the source region, we do not expect SEE from the thruster body to have an effect on device performance. Instead, our discussion of thruster body configurations focuses on conductivity.

Thruster Body Conductivity

In comparing the anodized and untreated thruster body, it is important to note that the anodization process does not result in a perfectly insulating body. This is evident from the fact that body floating potentials in the baseline configuration remain high, indicating that the body remains electrically tied to the radial walls of the source. Therefore, it is inaccurate to completely treat the anodized body as an insulator. Instead, we can model the effect of the anodization as a difference in the collection area of the body. Examining the current balance model presented in Fig. 21, we find that increasing the body collection area increases wall losses. Indeed, examining the efficiency modes presented in Fig. 20, mass utilization and energy efficiency both decreased in the untreated configuration. These results suggest good agreement between our current loss model and our experimental results. Therefore, we attribute the observed performance decrease with the untreated thruster body to an increase in loss currents to the large conductive area of the body.

VII. Conclusion

In this work we have presented an experimental investigation of wall material effects in an ECR magnetic nozzle thruster. We set out with a goal to evaluate several existing hypotheses relating to wall conductivity and secondary electron emission. To do so, we utilized a thrust stand and far-field plasma diagnostic suite to test various configurations of a 30 W class ECR thruster. We began by establishing a baseline configuration and characterizing global performance and the efficiency modes of the device at powers ranging from 20 W to 50 W. We then varied the material of the thruster radial wall, backplate, and body.

The thruster was tested with radial walls made of aluminum, graphite, boron nitride and alumina walls. We identified the general trend that the thruster performance was improved with insulating radial wall materials. From the efficiency mode analysis we found that the primary mechanism for the global performance increase was improved energy efficiency. In the next study, the backplate material was changed from boron nitride to alumina. This change to material demonstrated that performance is highly sensitive to the backplate material, as thrust decreased by over 50%. The results of the plasma diagnostics showed that the alumina backplate yielded lower mass utilization and lower energy efficiency. Finally, the material of the thruster body was changed from anodized to untreated aluminum. This change also corresponded to a decrease in performance. Once again decreased mass utilization and energy efficiency were identified as the cause of the lowered global performance metrics.

Finally, we compared our experimental results to the proposed physical effects of wall materials. From the radial wall material investigation it was found that there was evidence that secondary electron emission increased wall losses at higher powers. Additionally, insulating radial wall materials did appear to eliminate loss current pathways in the source. For the backplate study, it is possible that the performance discrepancy between alumina and BN could be explained entirely by SEE. However, we proposed an additional loss mechanism stemming from dielectric losses in the alumina. Finally, the study of thruster body material further confirmed the detrimental loss currents arising from conductive surfaces.

VIII. Acknowledgements

This work was supported by the Air Force Office of Scientific Research Space Power and Propulsion Program under grant award number FA9550-25-1-0025. The authors would like to thank Miron Liu, John Riley O'Toole, Dr. Parker Roberts, and Dr. Tate Gill for many useful discussions.

References

[1] "Civil space shortfall ranking," NASA SMTD, Tech. Rep., 2024.

[2] I. Levchenko and et al., "Space micropropulsion systems for cubesats and small satellites: From proximate targets to furthermost frontiers," *Applied Physics Reviews*, 2017.

[3] M. B. Belikov, O. A. Gorshkov, E. N. Dyshlyuk, A. S. Lovtzov, and A. A. Shagayda, "Development of low-power hall thruster with lifetime up to 3000 hours," *30th International Electric Propulsion Conference*, 2007.

[4] J. Jarrige, P.-Q. Elias, F. Cannat, and D. Packan, "Performance comparison if an ecr plasma thruster using argon and xenon as propellant gas," in *33rd International Electric Propulsion Conference*, no. 420, 2013.

[5] J. Jarrige and et al., "Characterization of a coaxial ecr plasma thruster," *AIAA Space Conference and Exposition*, vol. 2628, 2013.

[6] B. N. Wachs, "Optimization and characterization of facility effects for a low power electron cyclotron resonance magnetic nozzle thruster," Ph.D. dissertation, University of Michigan, 2022.

[7] A. J. Sheppard and J. M. Little, "Performance analysis of an electron cyclotron resonance thruster with various propellants," *Journal of Propulsion and Power*, vol. 38, no. 6, pp. 998–1007, 2022.

[8] V. Désangles, S. Peterschmitt, D. Packan, and J. Jarrige, "Ecra thruster advances, 30w and 200w prototypes latest performances," in *37th International Electric Propulsion Conference*. Electric Rocket Propulsion Society, 2022.

[9] T. Vialis, J. Jarrige, D. Packan, and A. Aanesland, "Direct thrust measurement of an electron cyclotron resonance plasma thruster," *Journal of Propulsion and Power*, 2018.

[10] A. J. Eckhaus and B. A. Jorns, "A model-driven investigation into the role of wall secondary electron emission in an electron cyclotron resonance magnetic nozzle thruster," in *38th International Electric Propulsion Conference*. Electric Rocket Propulsion Society, 2024.

[11] A. Simon, "Ambipolar diffusion in a magnetic field," *Physical Review*, vol. 90, No.2, 1955.

[12] A. Drentje, U. Wolters, A. Nadzeyka, D. Meyer, and K. Wiesemann, "Simon short circuit effect in ecris," *Review of Scientific Instruments*, vol. 73, no. 2, pp. 516–520, 2002.

[13] R. Geller, *Electron Cyclotron Resonance Ion Sources and ECR Plasmas*. Institute of Physics Publishing Bristol and Philadelphia, 1996.

[14] G. D. Hobbs and J. A. Wesson, "Heat flow through a langmuir sheath in the presence of electron emission," *Plasma Physics*, vol. 85, pp. 85–87, 1967.

[15] D. M. Goebel and I. Katz, *Fundamentals of Electric Propulsion: Ion and Hall Thrusters*. JPL Space Science and Technology Series, 2008.

[16] S. Peterschmitt and D. Packan, "Comparison of waveguide coupled and coaxial coupled ecra magnetic nozzle thruster using a thrust balance," in *36th International Electric Propulsion Conference*, no. 188, 2019.

[17] G. Crimi, A. Eckert, and D. Miller, "Microwave driven magnetic plasma accelerator studies (cyclops)," NASA, Tech. Rep., 1967.

[18] J. Sercel, "An experimental and theoretical study of the ecr plasma engine," Ph.D. dissertation, California Institute of Technology, 1993.

[19] M. A. Lieberman and A. J. Lichtenberg, *Principles of Plasma Discharges and Materials Processing*. John Wiley Sons, 2005.

[20] E. Ahedo and M. Merino, "On plasma detachment in propulsive magnetic nozzles," *Physics of Plasmas*, vol. 18, No. 053504, 2011.

[21] A. V. Arefiev and B. N. Breizman, "Magnetohydrodynamic scenario of plasma detachment in a magnetic nozzle," *Physics of Plasmas*, vol. 12, 2005.

[22] E. Hooper, "Plasma detachment from a magnetic nozzle," *Journal of Propulsion and Power*, vol. 9, No.5, 1993.

[23] S. Peterschmitt, "Development of a stable and efficient electron cyclotron resonance thruster with magnetic nozzle," Ph.D. dissertation, Institut Polytechnique De Paris, 2020.

[24] V. Baglin, J. Bojko, O. Grobner, B. Henrist, and H. N, "The secondary electron yield of technical materials and its variation with surface treatments," in *EPAC 2000, Vienna, Austria*, 2000.

[25] J. Cazaux, "Secondary electron emission yield: Graphite and some aromatic hydrocarbons," *Journal of Physics D: Applied Physics*, vol. 38, No. 14, pp. 2443–2445, 2005.

[26] S. Correyero, J. Jarrige, D. Packan, and E. Ahedo, "Plasma beam characterization along the magnetic nozzle of an ecr thruster," *Plasma Sources Science and Technology*, vol. 28, 2019.

[27] S. T. Hepner, "The influence of instabilities on the electron dynamics of a magnetic nozzle," Ph.D. dissertation, University of Michigan, 2022.

[28] R. B. Lobbia and B. E. Beal, "Recommended practice for use of langmuir probes in electricpropulsion testing," *Journal of Propulsion and Power*, vol. 33, 2017.

[29] L. L. Su, P. J. Roberts, T. M. Gill, W. J. Hurley, T. A. Marks, C. L. Sercel, M. G. A. C. B. Whittaker, E. Viges, and B. A. Jorns, "High-current density performance of a magnetically shielded hall thruster," *Journal of Propulsion and Power*, 2024.

[30] O. Hitchens, "Performance increase of electron cyclotron resonance magnetic nozzle thruster via magnetically thickened resonance region," Ph.D. dissertation, University of Surrey, 2025.

[31] D. L. Brown, M. Walker, J. Szabo, W. Huang, and J. Foster, "Recommended practice for use of faraday probes in electric propulsion testing," *Journal of Propulsion and Power*, vol. 33, No. 3, 2017.

[32] V. Desangles, F. Boni, E. G. Renaud Ferrand, P.-Q. E. Romain Pioch, and D. Packan, "Ecra thruster latest development at onera: Focus on thrust vectoring activities," *Aerospace Europe Conference*, 2023.

[33] G. C. S. Wensheng Huang, Rohit Shastry and H. Kamhawi, "Farfield plume measurement and analysis on the nasa-300m," NASA, Tech. Rep., 2013.

[34] W. Huang and R. Shastry, "Analysis of wien filter spectra from hall thruster plumes," *Review of Scientific Instruments*, 2015.

[35] T. Lafleur, "Helicon plasma thruster discharge model," *Physics of Plasmas*, vol. 21, 2014.

[36] Álvaro Sánchez-Villar, J. Zhou, E. Ahedo, and M. Merino, "Coupled plasma transport and electromagnetic wave simulation of an ecr thruster," *Plasma Sources Science and Technology*, 2021.

[37] D. Packan and et al., "H2020 minotor: Magnetic nozzle electron cyclotron resonance thruster," *36th IEPC*, 2019.

[38] M. R. Inchingolo, M. Merino, and J. Navarro-Cavallé, "Plume characterization of a waveguide ecr thruster," *Journal of Applied Physics*, 2023.

[39] P.-Q. E. Julien Jarrige, Sara Correyero and D. Packan, "Investigation on the ion velocity distribution in the magnetic nozzle of an ecr plasma thruster using lif measurements," *35th International Electric Propulsion Conference*, 2017].

[40] W. Haynes, D. R. Lide, and T. J. Bruno, *CRC Handbook of Chemistry and Physics*. Taylor and Francis Group, 2014.

[41] R. Vila, M. Gonzales, J. Molla, and A. Ibarra, "Dielectric spectroscopy of alumina ceramics over a wide frequency range," *Journal of Nuclear Materials*, 1998.

[42] "Dielectric constant and loss data," Air Force Materials Laboratory, Tech. Rep., 1977.